Imaging the Mariánské Lázně Fault (Czech Republic) by 3-D ground-penetrating radar and electric resistivity tomography

TOMÁŠ FISCHER[1,2], PETRA ŠTĚPANČÍKOVÁ[3], MAGDA KAROUSOVÁ[1], PETR TÁBOŘÍK[1], CHRISTINA FLECHSIG[4] AND MAHMOUD GABALLAH[5]

1 Charles University in Prague, Faculty of Science, Albertov 6, 128 43 Praha 2, Czech Republic (fischer@natur.cuni.cz)

2 Institute of Geophysics, Acad. Sci. Czech Republic, Boční II/1401, 141 31 Praha 4, Czech Republic

2 Institute of Rock Structure and Mechanics, Acad. Sci. Czech Republic, V Holešovičkách 41, Praha 8, Czech Republic

3 University of Leipzig, Institute of Geophysics and Geology, Talstrasse 35, D-04103 Leipzig, Germany

4 National Research Institute of Astronomy and Geophysics, 11722 Helwan, Cairo, Egypt

Received: April 1, 2012; Revised: June 25, 2012; Accepted: August 2, 2012

ABSTRACT

Geodynamic activity in the area of West Bohemia is typified by the occurrence of earthquake swarms, Quaternary volcanism and high flux of mantle-derived CO_2. The highest swarm activity occurs beneath the eastern edge of the Cheb basin, which is delineated by the NW-SE trending morphologically pronounced Mariánské Lázně Fault (MLF) controlling the formation of the basin. The previous trenching survey across the MLF zone has identified several fault strands with possible Quaternary activity. In this paper we present the results of the geophysical survey focused to trace the faults signatures in geophysical sections and to build an image of near surface tectonics. The method of electric resistivity tomography (ERT) along two profiles parallel to the trench identified a strong resistivity contrast between the bodies of sandy gravels in the middle and conductive clayey sands to the west and weathered crystalline basement to the east. The 2-D ground penetration radar (GPR) sections show direct correlation of reflections with lithological boundaries identified in the trench. As expected, the GPR signal amplitudes increase with the resistivities found in the ERT sections. Two of the four faults identified in the trench are indicated in the resistivity and GPR sections. A 3-D GPR measurement has identified a spot of high amplitudes elongated parallel to the MLF trend, which coincides with the high resistivity body. To improve the signal-to-noise ratio of the time slices we stacked the GPR time slices within vertically homogeneous blocks. This provided a contrast image of the sand-gravel body including its boundaries in three dimensions. The detailed analysis of the 3-D GPR cube revealed additional fault that limits the highly reflective sands and appears to be offset by another younger fault. Our results suggest a complex fault pattern in the studied area, which deserves a further study.

Keywords: fault tectonics, resistivity tomography, ground penetrating radar

1. INTRODUCTION

The NNW-SSE trending Mariánské Lázně Fault (MLF) zone is one of the most striking geomorphologic features in the western part of the Bohemian Massif. Its northern termination is usually referred as the Eastern Marginal Fault (EMF) of the Tertiary Cheb basin (*Špičáková et al., 2000*). The present geodynamic activity in area of Cheb basin is manifested in the form of earthquake swarms (e.g. *Horálek and Fischer, 2010*; *Fischer et al., 2010*) and ubiquitous emanations of mantle-derived carbon-dioxide (*Weinlich et al., 1998*). In this area, the NNW-SSE trending Mariánské Lázně Fault (MLF) intersects the main seismoactive zone of Nový Kostel (Fig. 1), where more than 80% of seismic energy

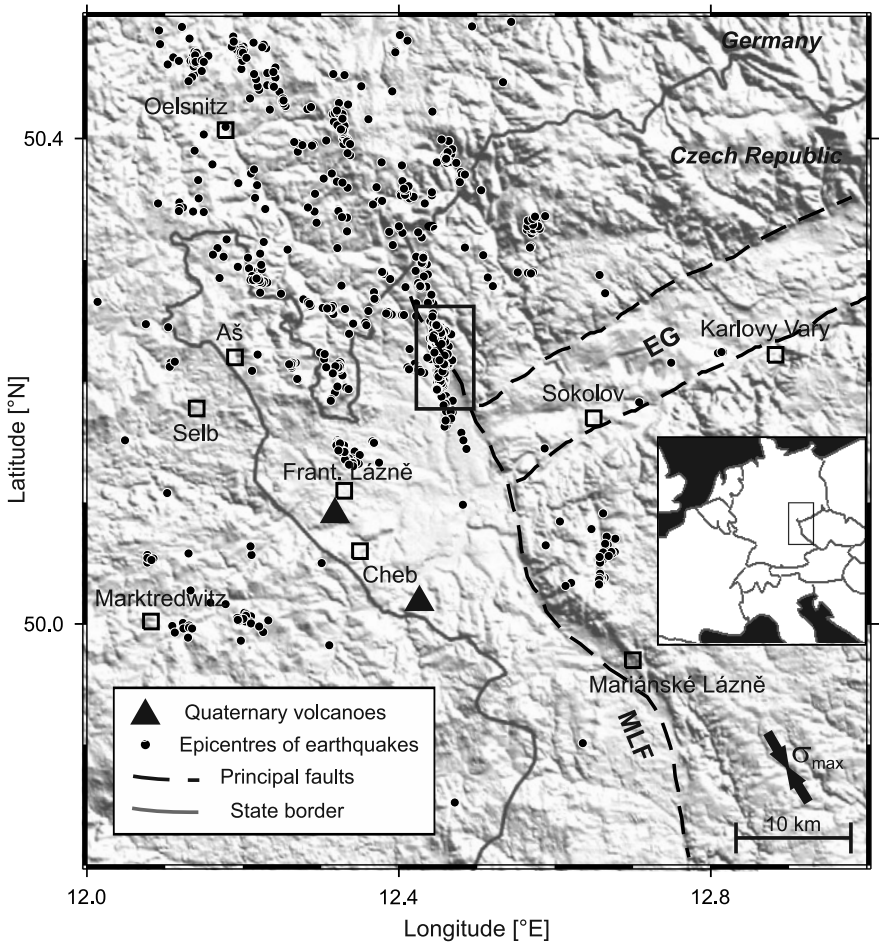

Fig. 1. Map of the West-Bohemia/Vogtland seismoactive area. The central rectangle indicates the area of interest, which is depicted in the inset of Fig. 2. Mariánské Lázně Fault (MLF) and Eger Rift (EG) are indicated by dashed lines.

has been released within the last 25 years (*Fischer and Michálek, 2008*). According to *Pitra (1999)* the fault zone originated in late-Variscan (380–300 Ma) as a normal fault with a dextral component. The normal character of the fault zone controlled the forming of the Cheb basin since late Eocene until Pliocene (*Špičáková et al., 2000*). The subsidence is preserved in the present-day topography with a well-expressed escarpment to the east, which is 50 to 400 m high. The Cheb basin is typified by a blocky fabric due to a network of faults of different strike. Besides the NNW and NW marginal faults *Špičáková et al. (2000)* identified also faults trending NE, E-W and N-S. *Bankwitz et al. (2003)* underlined the present-day significance of the N-S faults and suggested that the roughly N-S striking Počátky-Plesná Fault Zone (PPZ) delineated by the valley of the Plesná river is associated with the hypocenters of earthquakes, which strike about 170° in the Nový Kostel area (*Fischer at al., 2010*). The recent study of *Peterek et al. (2011)* documents neotectonic activity of the Cheb Basin area where MLF branches in four individual segments and interprets the PPZ as a sinistral wrench zone. The area is also typified by Quaternary volcanism represented by Komorní Hůrka, Železná Hůrka and newly discovered maar structure of Mýtina (*Mrlina et al., 2009*).

Near surface tectonics could be studied by various geophysical methods. Electromagnetic, seismic and gravity methods are found the most suitable for investigating the blocky fabric of the area. The electromagnetic methods are sensitive to lateral and vertical changes of electric resistivity and permittivity of materials, which are affected by moisture changes and clay contents of subsurface deposits and rocks. While refraction seismics is able to identify zones of decreased seismic velocities accompanying the fault zones, reflection seismics identifies subhorizontal lithology interfaces. The gravity methods enable identifying blocks of different densities, which are often limited by faults. Sub-surface expressions of faults are studied using ground penetrating radar (GPR) method alone (*McClymont et al., 2009*; *Dentith et al., 2010*; *Pauseli et al., 2010*) or in combination with electric resistivity tomography (ERT), by ERT with gravimetry (e.g. *Štěpančíková et al., 2010, 2011*) or by resistivity profiling (*Valenta et al., 2008*). Alternatively also a combination of GPR and high-resolution reflection seismics can be used successfully for delineating subsurface patterns of faults (*Chow et al., 2001*). In Cheb Basin, several geophysical surveys have been carried out. Gravity map shows that the EMF is expressed by steep gravity gradient and that the negative gravity anomaly correlates well with the sedimentary depocenter of the basin (*Mlčoch and Skácelová, 2009*). The ERT studies of *Flechsig et al. (2010)* revealed a minor graben-like structure close to the eastern margin of the basin with vertical displacements of 10–15 m. A GPR survey and small trench survey across two segments of MLF close to Nový Kostel indicated a recent tectonic reactivation of the fault (*Kämpf et al., 2005*).

In this study, we focus on the Eastern Marginal Fault of the Cheb Basin, where a recent paleoseismologic trenching survey has identified Late Quaternary activity (*Štěpančíková et al., personal communication*) within the zone. We carried out an electrical resistivity tomography and 3-D georadar survey to trace the faults signatures in geophysical sections and to extend the ground truth data in the broader vicinity of the trench.

2. THE STUDIED SITE

The study locality is situated at the mountain front line of the Krušné hory Mts. controlled by the MLF (Fig. 1). Due to lack of fault outcrops, the trenching site was chosen based on the geomorphologic analysis, which suggests that the fault trace occurs at the point where series of sub-parallel valleys become deeply incised into an apparently uplifted blocks and that it controls the most recent morphology of the marginal slope. The site lies between the villages Nový Kostel and Kopanina within the Eastern Marginal Fault of the Cheb Basin (Fig. 2). The trench of 100 m length had an azimuth of 62° and reached the depth of 1.5 to 2.5 m. It exposed a succession of sedimentary units, whose lithologies are briefly described downhill southwestwards as follows (Figs 3 and 5 top):

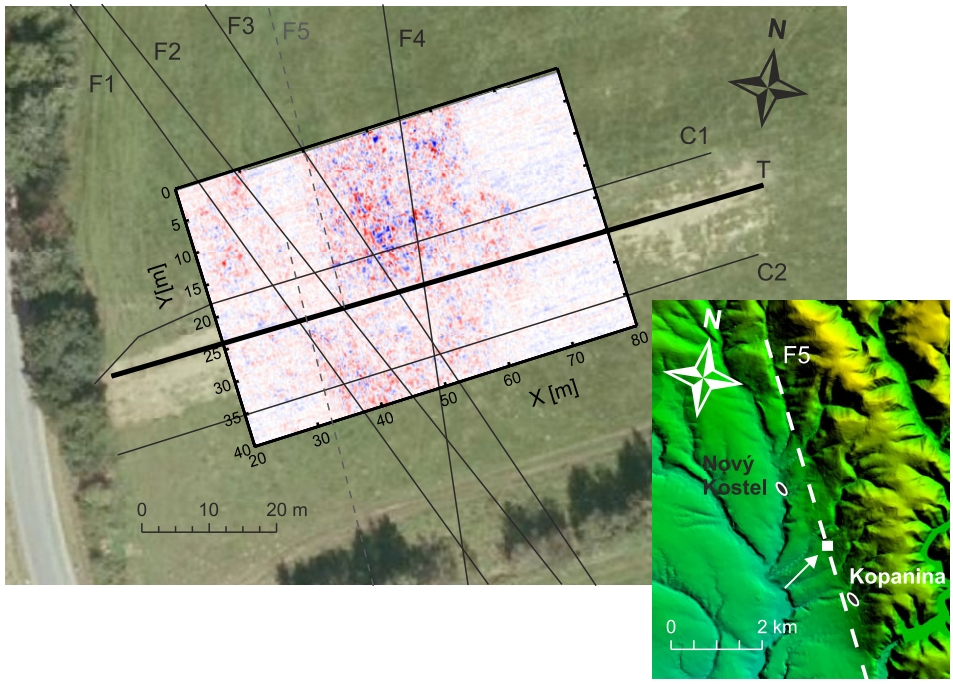

Fig. 2. Detailed situation of the investigated area. Profiles C1 and C2, trench contours T and the rectangular area of the 3D georadar survey are indicated. The azimuth of the *X*-coordinate is 62°. The presumed course of faults F1, F2, F3 and F4 was derived from the trench survey. The time section corresponds to the two-way time of 50 ns (depth about 2.2 m; blue and red correspond to negative and positive amplitudes, respectively). The inset shows the location of the survey area at the eastern margin of the Cheb Basin with the investigated area indicated by arrow, and the trend of fault F5 derived from analysis of the 3-D GPR survey.

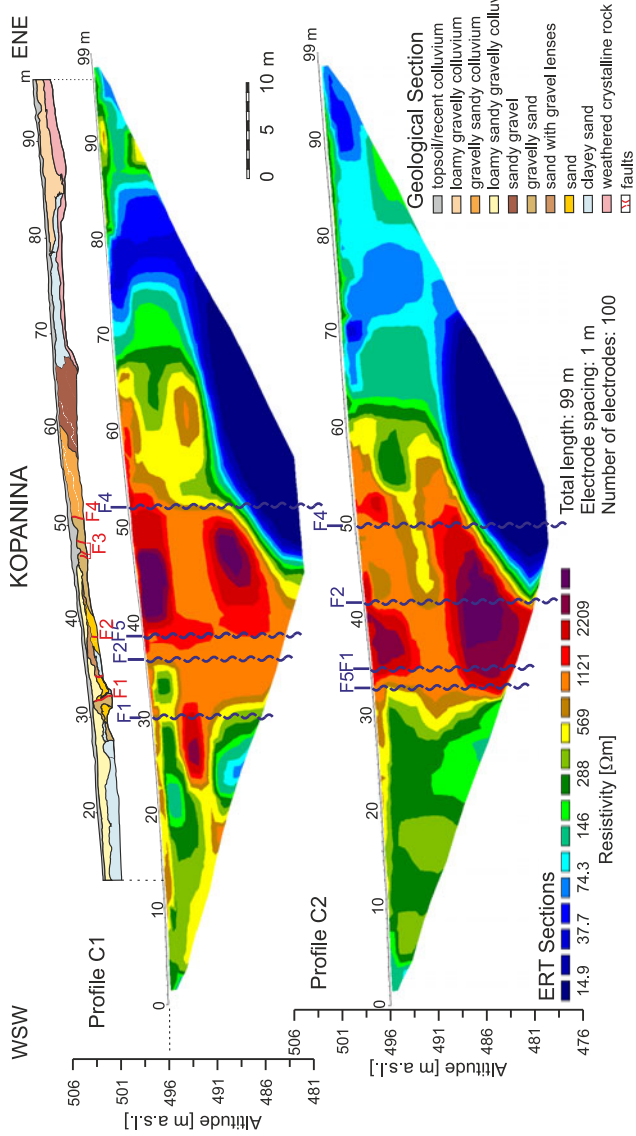

Fig. 3. Lithologic section along the trench and electric resistivity tomography (ERT) sections (obtained by robust inversion) along profiles C1 and C2. Wavy lines indicate position of the faults F1, F2 and F4 extrapolated from the trench. The profile C1 was situated 5 m NW from the trench and the profile C2 was 10 m SE from the trench. The *RMS* error after five iterations was 4.0% for profile C1 and 5.7% for profile C2.

between $X = 97$ and 78 m fluvio-colluvial sandy deposits with cobbles fill the depression in clayey-sandy colluvial sediments, which cover completely disintegrated, chemically weathered crystalline basement. Between $X = 66.5$ and 51 m inclined beds of heterogeneous units of sandy gravels with clayey silty matrix and reworked gravelly sands with fragments of ferricretes overlay the basement. This formation is terminated by the fault F4 striking at 162° at $X = 51$ m. The following so-called Vildstein Formation is formed by diagonally stratified fine gravels and sands. These sediments are disturbed by minor subparallel 137°–142° striking normal faults (F3) between $X = 48$ and 45 m. Up to 45° tilted heterogeneous layers of overlying fine gravels and sands are cut by subvertical fault F2 with strike of 132° at $X = 38.5$ m, which is accompanied by distinctive iron mineralization. The following layers of clayey sand to clay are downwarped and deformed by the youngest 134° striking fault F1 at $X = 32$ m, which separates them from deformed stratified coarse sands to the southwest. Between $X = 13$ and 26 m clayey sand to clay is overlain by loamy gravelly colluvium.

3. DATA ACQUISITION AND PROCESSING

The geophysical surveys were carried out one year after the trench has been earthed up. The aim was to extend the fault geometry derived from the trench survey horizontally and also vertically. Two profiles were located parallel to the trench (Fig. 2); the profile C1 (99 m long, at the distance of 5 m to the NNW) and profile C2 (207 m long, at the distance 10 m to the SSE). Electrical resistivity was measured by the multi-electrode method using the electrode spacing of 1 m. The profile C2 was then used for a 2-D GPR measurement using a 250 MHz shielded antenna.

For the maximum consistency between the two ERT profiles, only the first 99 m of the resistivity data on profile C2 were used for the inversion by the RES2DINV software package (*Loke, 1996*) using standard least-square inversion with 5 iterations. The decrease of resolution on the right edge of the profile due to limiting the inversion only to the left part of the profile is acceptable because we are interested mainly in the central part of the profile where the tomograms overlap with the GPR cube and the fault traces mapped in the trench. A negligible fraction of unreal data points (1.9% for profile C2 and none for profile C1) was removed by means of the *RMS* statistics. Topography was measured by a total station and final apparent resistivity models thus include topographic corrections. Additionally, the original data sets were also processed by robust inversion (applied to both the data and model with data constraint cut-off factor 0.05), which is less detailed, but offers simplified image of the subsurface situation. This model is usually more accurate in detection of the boundaries between two neighbouring structures. The robust inversion is also less sensitive to geoelectric noise.

The 3-D GPR measurement was carried out by a 250 MHz shielded antenna in a 40 m wide rectangular area composed of 161 profiles, each of 60 m length. To choose the optimum resolution a test profile was measured also by antenna with nominal frequency of 100 MHz. The cross-line and in-line spacing was 25 cm and 6 cm, respectively. The rectangular area was geodetically delineated by a total station. To keep the precise antenna positioning, a network of strings was used to guide the antenna motion; the inline distance was permanently controlled by comparing the distance measured by the wheel with the

string network and if necessary a correction was introduced. The GPR measurement was carried out within two subsequent days with stable warm weather, which assured stabilized moisture conditions of the subsurface soil layer. The surveyed area was a meadow with cutgrass, which provided optimum conditions for GPR signal transfer to the ground. The measurement started at the southeastern edge of the investigated area with forth and back antenna advance along the profiles. Data acquisition parameters were: sampling frequency of 3840 MHz, 577 samples per trace and 8 stacks.

The GPR data were processed using the ReflexW software. The 2-D processing included dewow filter, amplitude scaling, static correction (alignment of first arrivals), background removal, band-pass filtering in the range 50–350 MHz, running average (muting air and ground waves) and interpolation of 3 adjacent traces to obtain the same number of traces per profile.

We estimated the velocity of electromagnetic waves for converting the time slices to depth slices in two steps. First, the diffraction hyperbolae gave an estimate of the velocity in the range from 0.08 to 0.09 m/ns. Next we constrained the velocity by tracking the occurrence of the trench in subsequent time slices of the finally processed 3-D data. The trench is indicated in time slices by an *X*-delineated belt of smaller amplitudes at $Y = 25–26$ m (Fig. 4) due to GPR signal attenuation in the trench filling composed of disintegrated material with higher conductivity due to increased water content. The trench becomes invisible in the GPR slices for the two-way times larger than 44 ns. Considering the maximum prevailing depth of the trench of about 2 m this gives the wave velocity of 0.09 m/ns, which matches the upper bound of velocity estimated from the diffraction hyperbolae.

The GPR time slice in Fig. 2 shows high reflectivities in the central part of the investigated area that extends over almost the whole time/depth range. This is easily found using the animated view of subsequent time slices. In order to present this volume information in static plots we separate the investigated depth range into few quasi-homogeneous intervals, which are presented separately. First we improve the coherency of adjacent traces in all three directions by a 3-D *x*-*y*-*t* filter that also helps to decrease the random noise. The optimum length of the Hamming window filter was determined empirically as $3 \times 3 \times 3$ data points. In place of 2-D *x*-*y* filtering that is commonly used in 3-D GPR processing (e.g. *McClymont et al., 2009*) we applied a 3-D filter in order to take into account the possible correlation of inclined reflections in the full space. Next, we choose time intervals with self-similar time slice images and stack them. This is motivated by the fact that, according to the trench survey, the investigated faults and associated structures are subvertical. Hence the fault signatures are expected to be correlated in the adjacent time slices and a suitable kind of stacking is expected to increase the amplitude of reflections in the areas where reflections occur on top of each other. Before summation, the radargram amplitudes were converted to a suitable attribute in order to remove the polarity. To this purpose we tested different norms as the $L1$ (sum of absolute values), $L2$ (root-mean-square) and *MAX* (maximum of the absolute) norms. The results were found comparable and the $L2$ norm was chosen for final processing because of the slightly higher signal to noise ratio provided. The effect of filtering and stacking of time slices is illustrated in Fig. 4. The standard time slice showing the signed radargram amplitudes (Fig. 4a) is converted to absolute values with no filter (Fig. 4b), or after using a $3 \times 3 \times 3$

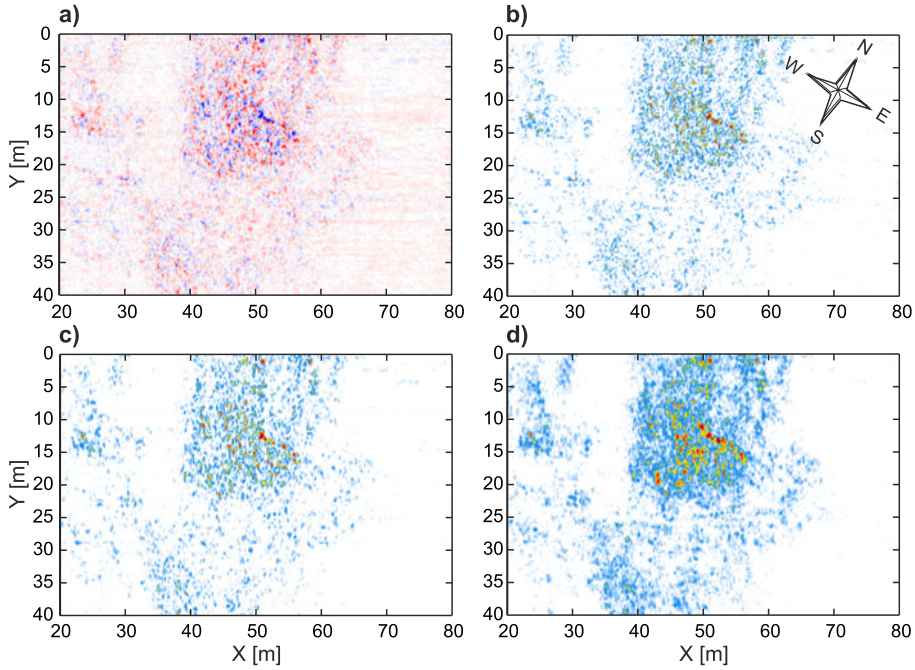

Fig. 4. Example of processing the 3D GPR time sections. **a)** The signed amplitudes (blue for negative, red for positive); **b)** absolute values of amplitudes; **c)** absolute values of amplitudes after using a 3 × 3 × 3 point *x*-*y*-*t* filter. Time section at 44.5 ns two-way-time is shown in a), b) and c). **d)** Stacked root-mean-squared amplitudes ($L2$ norm) for the two-way time interval from 39.3 to 52.1 ns after using a 3 × 3 × 3 point *x*-*y*-*t* filter. In b), c) and d) the colors from white to red show amplitudes from zero to maximum.

point *x*-*y*-*t* filter (Fig. 4c). Note the higher contrast of reflections due to filtering. Finally the $L2$ norm of amplitudes was stacked (Fig. 4d) in a window of 13 ns length centered at the time slice shown in Figs 4a–c. The optimal time window for summation was chosen so that it represents a homogeneous depth range with unchanged time-slice image.

4. RESULTS OF GEOPHYSICAL MEASUREMENTS

The resistivity sections (Fig. 3) obtained by robust inversion showed better pronounced resistivity contrasts than standard inversion scheme. A high-resistivity body occurs in the central part of both profiles C1 and C2, which are situated 15 m apart. However, the detailed structure differs significantly, namely in terms of the shape of the high-resistivity body boundaries. We benefited from the lithologic section in Fig. 3 to disclose the origin of the resistivity heterogeneities. A better correlation is found between the lithology and resistivity section along the profile C1, which is situated only 5 m NNW from the trench. It turns out that the high-resistivity body ($\rho > 800$ Ωm) corresponds to a shallow layer of sandy gravels and reworked gravelly sands between $X = 64$ and 49 m

and to a thicker unit of fine gravels and sands of the Vildstein formation between $X = 49$ and 35 m. The low resistivities of 20 to 200 Ωm at $X > 64$ m pertain to the fluvio-colluvial sandy deposits overlaying chemically weathered crystalline basement showing the lowest resistivities of less than 20 Ωm. The medium resistivities of 200 to 800 Ωm for $X < 35$ m correspond to loamy gravelly colluvium on top of clayey and coarse sands. The profile C2, which is situated 10 m south-east from the trench shows quite similar resistivity section with more pronounced vertical boundaries between the quasi-homogeneous blocks.

Four faults are indicated in the resistivity sections. The faults F1, F2 and F4 were identified in the trench, whereas F5 was derived from the GPR survey (see Section 5). The faults intersection with profiles C1 and C2 was derived from their strike measured in the trench. Among them, F1 and F4 are best reflected in the resistivity contrast, which is discussed below in Discussion.

The GPR section in Fig. 5a is parallel to the trench, 0.75 m to the NW. It is characterized by strong reflections in the middle of the profile ($X = 32–60$ m), weak reflections on the left and almost missing reflections on the right. This corresponds directly to the resistivity distribution in the ERT section - see e.g. the highest GPR amplitudes around $X = 45$ m where also the resistivity maximum occurs. The overlaid lithology section and GPR section show striking correlation even in details, which confirms that the wave velocity 0.09 m/ns used for conversion from time to depth sections was correct. Note the missing reflections in the lowermost layer of clayey sands at $X < 27$ m and at $X > 66$ m or the inclined stratigraphy expressed in the reflections elsewhere. While the faults F2 and F4 limit from both sides the high reflectivity body, the fault F1 is expressed as the left limit of the medium reflections between $X = 32$ and 38 m; note also the vertical belt of zero amplitudes along F1, probably due to deformed material within the fault zone with weak reflectivity.

The correlation of high resistivities and strong GPR reflections (Fig. 6) sheds light on the origin of the reflections. In terms of resistivity, three quasi-homogeneous blocks could be delineated in the depth range of GPR (0–6 m) in Fig. 5a. In the uphill (ENE) direction, these include: (1) low resistivities of about 200 Ωm for $X < 32$ m; (2) high resistivities of about 1000 Ωm for $X = 32–58$ m; (3) low resistivities of about 80 Ωm for $X > 58$ m. These intervals coincide well with the weak GPR reflections on the left, strong GPR reflections in the middle and almost missing GPR reflections on the right. Comparison with the lithologic profile shows that the strong reflections are associated to gravels and sands of the Vildstein formation, while the very low amplitudes on the left and right occur due to the high GPR signal attenuation in the clayey material found in these areas. Knowledge of resistivity ρ of the quasi-homogeneous blocks enables to estimate the signal attenuation that is usually characterized by the skin depth δ, which is the distance where the amplitude of the electromagnetic wave is reduced by factor of $1/\mathrm{e}$; $\delta = 1/\alpha$. The coefficient of absorption

$$\alpha = \omega \sqrt{\frac{\varepsilon\mu}{2}\left(\sqrt{1+\left(\rho\omega\varepsilon\right)^{-2}}-1\right)} \tag{1}$$

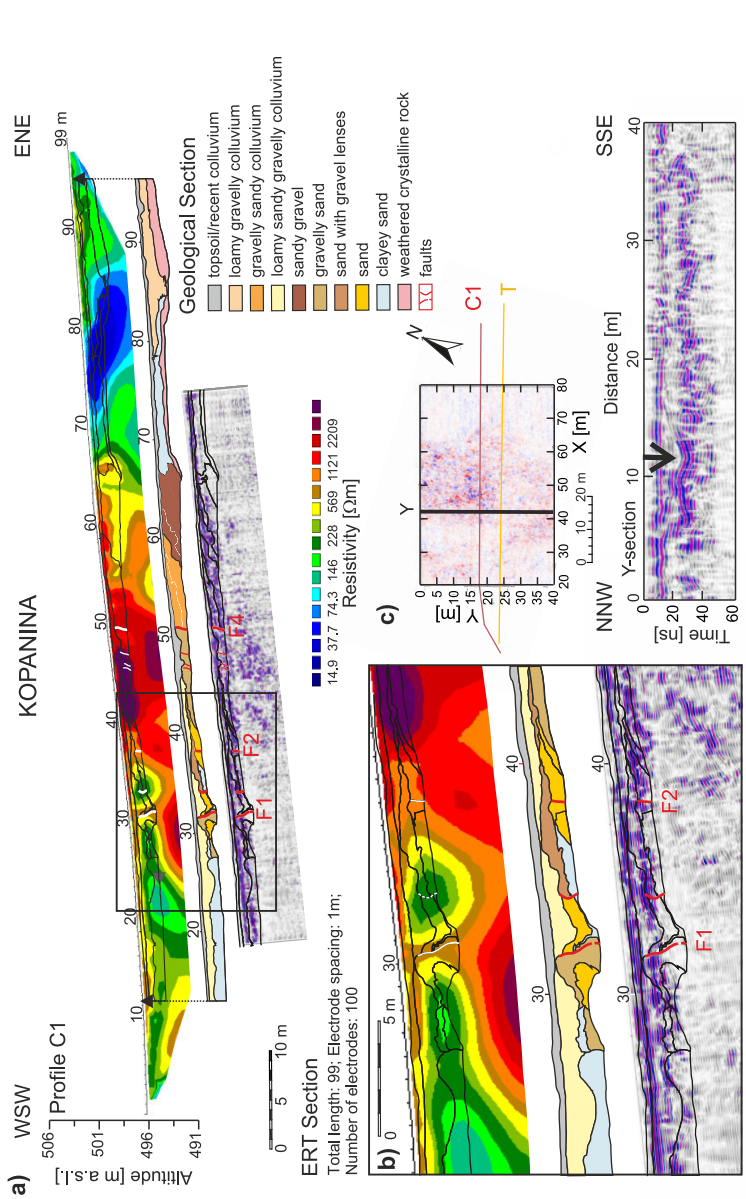

Fig. 5 **a)** Electric resistivity tomography (ERT) section (upper 6 m), lithologic section and ground penetrating radar (GPR) sections along the trench; **b)** the detail in the area of fault F1; **c)** a GPR section across the trench (along *Y* axis); note the morphology of the buried paleochannel around $Y = 10$ m (black arrow). The position of faults in a) and b) is taken from the trench survey. The ERT profile C1 was situated 5 m NW and the GPR profile 0.75 m NW from the trench. The lithologic section is thus shifted in a) and b) by 1.5 m SW so that the youngest fault F1 overlaps in all three sections. The ERT sections were processed by standard inversion included in Res2Dinv, which gave *RMS* error of 1.9% after five iterations.

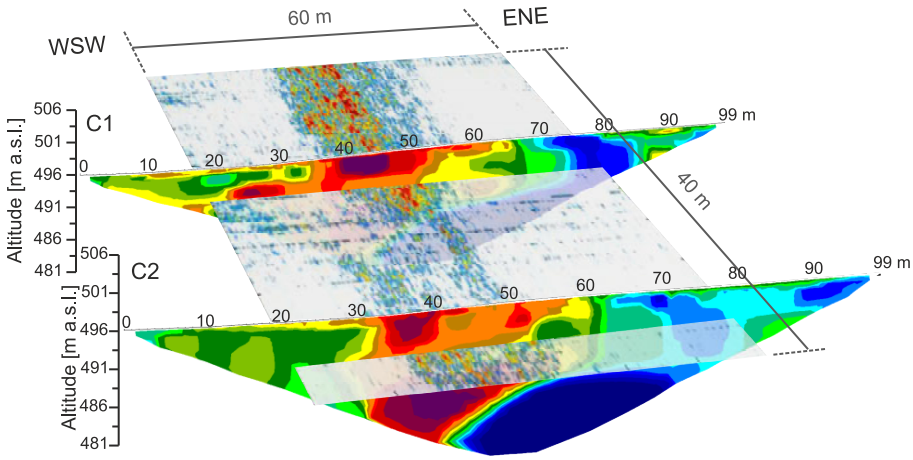

Fig. 6. Intersection of the two ERT profiles and the GPR time slice corresponding to the depth of 5 m. Note the striking correlation between the high resistivity and high reflectivity of the material in the centre of the profiles. See Fig. 3 for the color scale of resistivities and Fig. 4 for the color scale of the GPR time slice.

depends on the angular frequency ω, permittivity ε and permeability μ (e.g. *Cassidy, 2009*). To obtain estimate of relative permittivity $\varepsilon_r = \varepsilon/\varepsilon_0$ we use the tabulated values from 10 to 30 for wet sand and from 15 to 40 for wet clay. Additional constraint is the wave velocity of 0.9 m/ns, which depends on permittivity as $v = c/\sqrt{\varepsilon\mu}$ and gives $\varepsilon_r = 11$. For the antenna frequency 250 MHz one gets the skin depth of 3.5 m in the left, 17.7 m in the central and only 1.4 m in the right quasi-homogeneous block (Table 1). This proves that the high GPR amplitudes in the middle of profile C2 are caused by small GPR signal attenuation in this area and that the reflections correspond to permittivity contrasts within the gravels and sands in this lithologic unit.

By stacking adjacent GPR time slices five quasi-homogeneous depth intervals showing distinct patterns of GPR amplitudes (Fig. 7) have been delineated.

- The first layer down to 0.8 m is typified by chaotic pattern of reflections from shallow subsurface affected by soil cultivation.
- The underlying block from 0.8 to 1.6 m depth shows several bright spots at $X = 40$–55 m and few smaller spots for $X = 25$–35 m, which are distributed along the expected trend of the fault F1. The trench is clearly visible as a belt of small amplitudes.
- The third layer at the depth interval from 1.6 to 2.2 m shows in general smaller amplitudes and a smaller lateral extent of the strong reflections, both in the left and right parts of the image.
- The fourth layer from 2.2 to 4.0 m depths displays increased noise and a different pattern of reflections. While the fault-associated reflections have significantly

Table 1. Penetration depth of the GPR wave for the 250 MHz antenna for the three quasi-homogeneous blocks.

X-Coordinates [m]	Lithology in the Trench	Resistivity [Ωm]	Relative Permittivity	Penetration Depth [m]
0–32	Clay, clayey sands	200	11	3.5
32–58	Sands, gravels	1000		17.7
58–99	Clayey sands, mica schists	80		1.4

decreased, the bright spot reflections on the right have filled the whole range of *X* interval from 40 to 65 m.

- The deepest layer shows a narrowed belt of high amplitudes on the right, on account of the shift of their right boundary by 5–10 m. Here, the fault-associated reflections have disappeared.

5. INTERPRETATION OF THE GEOPHYSICAL DATA AND DISCUSSION

Four main faults F4, F3, F2, and F1 with strike azimuths of 162°, 137°–142°, 132°, and 134°, respectively, were identified in the trench (Fig. 2). The GPR time slice in Fig. 2 shows a striking spot of high amplitudes in the central-upper part ($X = 40–60$ m, $Y = 0–20$ m) of the figure, which corresponds in general to gravels and sands. The uneven eastern limit of this body might reflect the lithological boundary. Fault F4, which bordered the Vildstein formation in the trench is apparent in particular at the stacked GPR time-slices of the depth interval 4 to 6.2 m, where it roughly coincides with the eastern limit of stronger reflections at about $X = 52$ m (Fig. 7f). This limit runs through the ERT profile C1 at $X = 52$ m, where it coincides with horizontal resistivity gradient at the depths from 4 to 11 m. Based on the measured strike, the fault F4 is supposed to cross the profile C2 at $X = 50$ m, where however it does not show any clear expression (Fig. 5).

The discussed spot of high amplitudes terminates on the west at $X = 38$ m by a striking rectilinear boundary of 155° azimuth for the depths higher than 1.6 m. No fault of similar strike matching this boundary was observed in the trench. The assumed fault could have been missed probably due to insufficient depth of the trench itself at that point (1.5–2 m), where it might have been covered by younger deposits or due to coincidence with another crossing fault of different strike and sense of motion, the fault F2. Nevertheless, the occurrence of a fault that would form this boundary is indicated by several different observations. Firstly, the logged geological structures in the trench as well as in the GPR sections along *X*-axis show that this boundary terminates the downwarped sedimentary layers/inclined subhorizontal reflections (at between $X = 42$ and 45 m in Fig. 5b). Secondly, 2-D GPR cross-sections along *Y*-axis show a geometry of a fluvial channel (diagonal bedding) around $Y = 10$ m, which indicates southwest direction of a river flow. This paleochannel is just terminated by that perpendicular boundary and does not occur in 2-D GPR cross-sections NW of the boundary (Fig. 5c). Thirdly, the rectilinear boundary

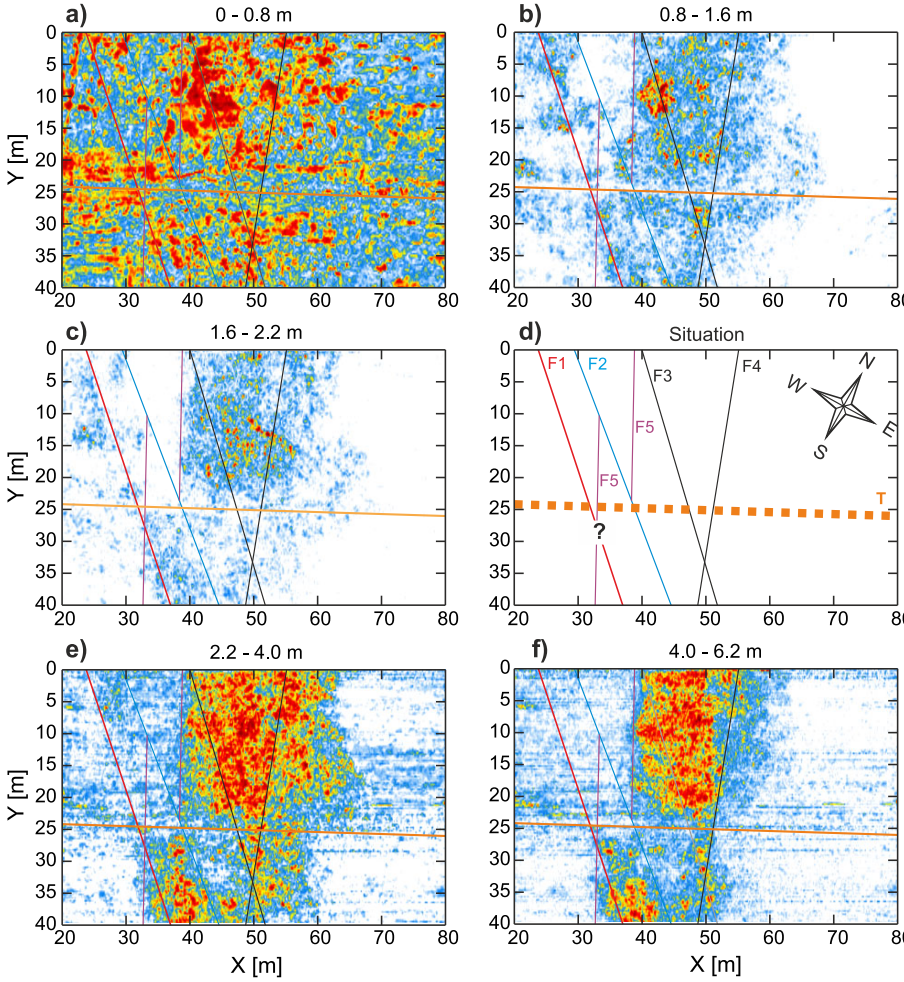

Fig. 7. Depth sections obtained as a sum of radargram attributes for several depth intervals (panels a, b, c, e, f). The position of the trench and trend of the faults extrapolated from the trench (F1, F2, F3, F4) and fault F5 interpreted from the GPR depth sections are shown in d). The color scale is the same as in Fig. 4.

coincides with a several kilometres long very probably fault-controlled morpholineament, which includes a rectilinear valley and rectilinear foot of hillslopes (see inset in Fig. 2). In addition, this fault (F5) is suggested in ERT profiles where it limits two sandy-gravel bodies of highest resistivity lying on top of each other (Fig. 3). Therefore, we consider this boundary expressed in GPR time-slices as a fault, which strikes at 155°.

However, as shown by GPR time-slices in Figs 7 and 8, this pronounced boundary along the suggested fault F5 is shifted in the southern half of the 3-D GPR surveyed area to the west by about 5 m. This shifted boundary corresponds to the pronounced resistivity

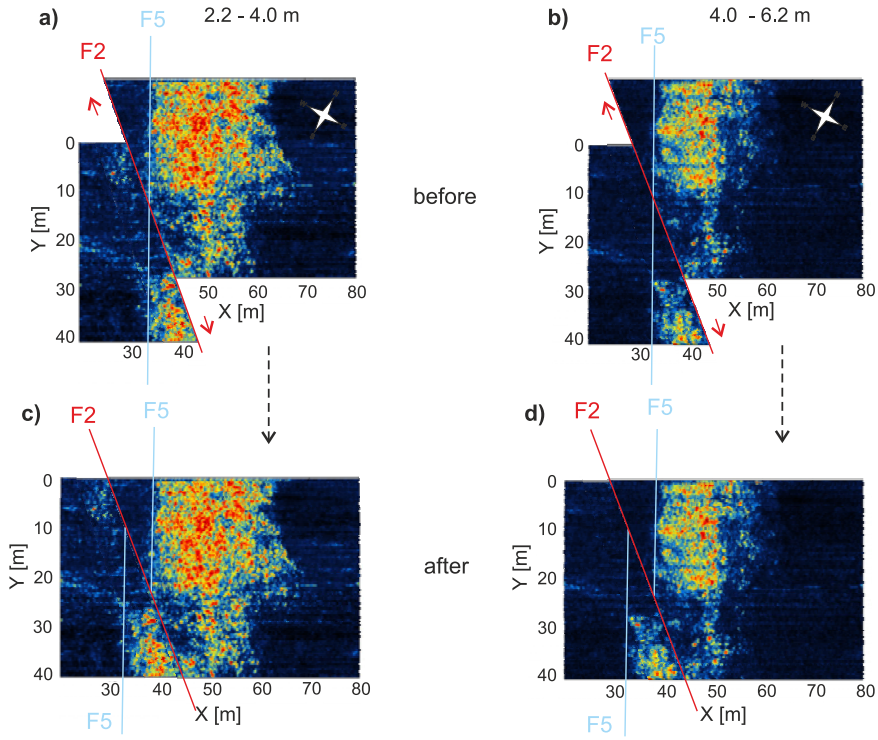

Fig. 8. Tectonic interpretation of the discontinuous western margin of the high reflectivity body by displacement along the fault F2. The stacked GPR blocks for the depth intervals: **a)** 2.2–4.0 m and **b)** 4.0–6.2 m. The colors from black to red show amplitudes from zero to maximum.

gradient at the profile C2 at $X = 33$ m (Fig. 3). A feasible explanation for this shift could be a right-lateral movement along the oblique fault F2 striking at 132° (Fig. 8). A strike-slip component of the movement along F2 was anticipated from the structural analysis in the trench, however, with unknown sense. The right-lateral component of the movement could have been a local response of this particular segment of the MLF zone to the maximum principal stress, which varies even recently around NW-SE direction (*Vavryčuk, 2011*; *Havíř, 2000*; *Seht et al., 2006*; *Bankwitz et al., 2003*), although in general MLF zone has been described as a left-lateral strike-slip fault zone during Plio-Quaternary (*Špičáková et al., 2000*; *Bankwitz et al., 2003*; *Peterek et al., 2011*). In addition, the indication that the movements along F2 probably postdate the activity of F5, so that F2 offsets the fault plane of F5, could be inferred from the trench and GPR time-slices, where F2 appears to be buried by thinner (younger) deposits than F5.

The presumed trend of fault F2 derived from the measured strike in the trench appears to limit the scattered spots of reflections from the NE (NW part of surveyed area in Figs 2, 7, and 8), which could have been a result of juxtaposition of different lithological bodies being offset by the fault. The trend of F2 should cut the ERT profile C2 at $X = 42$ m, which corresponds to the eastern limit of the high-resistivity body (Fig. 3). In contrast, in

profile C1 the fault F2 coincides with the eastern limit of the low-resistivity body at $X = 36$ m, which seems to correspond with clayey sands observed in the trench. In the NW part of the surveyed area, the GPR time-slices suggest that those reflections scattered along F2 trend are also limited on the SW, which is particularly apparent from the depths of 1.6 to 4 m (Figs 2 and 7). This coincides with the position and trend of the youngest fault F1 measured in the trench as well as derived from its topographical expression. In the ERT profile C1 (Fig. 3) at $X = 30$ m the fault F1 seems to divide the low-resistivity body to the depth of 2.5 m and then it makes the NE limit of the high-resistivity body of probably gravelly sands up to the depth of 6 m. Below this depth, in the upper 2.5 m, then it limits the high-resistivity probably gravelly sands to the NE to up to 6 m and more deeply the fault is expressed by a horizontal resistivity gradient of opposite direction. In C2, the fault F1 corresponds to the western limit of the high-resistivity body at $X = 35$ m. According to the trench survey, also the fault F1, with a strike of 134° (similar to that one of F2), was observed to have a strike-slip component of unknown sense of movement. In this case, the 3-D GPR time-slices have not shown any striking offset that would indicate the certain sense of movements, although the similar strike to F2 would imply also right-lateral movements. To support this idea, lateral extension of further 3-D GPR survey would be helpful.

As discussed above, the scattered spots of reflections in the NW part of the surveyed area in Fig. 7 are limited by faults on each side. The increased reflectivity of the material points to an impedance contrast between the overlying deposits and the reflective material, and to small signal attenuation, similar to the reflections related to the high-resistivity body. It seems probable that the spots are of the same origin as the reflections generated by the high-resistivity body, i.e. they correspond to the high-resistivity gravely sands found in the trench between $X = 38$ m and 52 m.

6. CONCLUSIONS

The presented study combines the methods of electric resistivity tomography and 3-D ground penetrating radar supplemented by geological information from the trenching survey to build an image of near-surface tectonics within the Eastern Marginal Fault of the Cheb Basin, which forms a northern portion of the Mariánské Lázně Fault. The trench has exposed a succession of sedimentary units, which cover chemically weathered crystalline basement. In the SW part of the trench the full depth of the section uncovered diagonally stratified fine gravels and sands of the Vildstein formation, which is disturbed by several faults. The geophysical measurements were conducted in order to extend the lithological and structural image laterally and depthwards. Their results combined with the ground truth information from the trench can be summarized as follows:

- Two ERT profiles parallel to the trench showed heterogeneous sections with strong resistivity contrast between the bodies of sandy gravels in the middle and conductive clayey sands to the WSW and weathered crystalline basement to the ENE.
- The 2-D GPR sections parallel to the trench show direct correlation of reflections with lithological boundaries identified in the trench. As expected, the signal amplitudes increase with the resistivity found in the ERT sections.

- The 3-D GPR measurement identified a spot of high amplitudes elongated parallel to the MLF trend, which coincides with the high resistivity body. We explain the high reflectivity by high impedance contrasts and small electromagnetic attenuation in the sandy material.
- A novel approach for processing the 3D GPR data was applied in order to improve the signal-to-noise ratio of the time slices and visualize the 3-D data. It consists in stacking of time slices within vertically homogeneous blocks of studied rock volume.
- Among four faults identified in the trench two of them (F1 and F4) are expressed in the resistivity and GPR sections. A detailed analysis of the 3D GPR cube has revealed additional fault F5 subparallel to F4 that limits the highly reflective sands and appears to be offset by a younger fault F2. Based on the strike, two families of faults can be distinguished: F1, F2, F3 striking parallel to the MLF (132°–142°) and F4, F5 striking about 155°–162°, which is close to the strike of the recent hypocenters (170°).

Our results suggest a complex fault pattern in the studied area, which deserves a further study with the aim to extend the depth and lateral range of the geophysical survey.

Acknowledgements: The work was supported by the Grant Agency of the Academy of Sciences of the Czech Republic, project No. IAA300120905 and the Czech Ministry of Education project No. MSM0021620855 and elaborated within the Institute Research Plan of IRSM Czech Academy of Sciences No. AVOZ30460519. The authors are grateful for fruitful discussions with Andreas Peterek, Petr Rojík, Čestmír Tomek, Jiří Dohnal and Jan Vilhelm. We thank also two anonymous reviewers for their helpful comments. We thank the landowner of the surveyed area, David Zelenka for the permission of our survey.

References

Bankwitz P., Schneider G., Kämpf H. and Bankwitz E., 2003. Structural characteristics of epicentral areas in Central Europe: study case Cheb Basin (Czech Republic). *J. Geodyn.*, **35**, 5–32.

Cassidy N.J., 2009. Electrical and magnetic properties of rocks, soils and fluids. In: Jol H.M. (Ed.), *Ground Penetrating Radar: Theory and Applications*. Elsevier B.V., Amsterdam, The Netherlands, 41–72, ISBN: 978-0-444-53348-7.

Chow J., Angelier J., Hua J.-J., Lee J.-C. and Sun R., 2001. Paleoseismic event and active faulting: from ground penetrating radar and high-resolution seismic reflection profiles across the Chihshang Fault, eastern Taiwan. *Tectonophysics*, **333**, 241–259.

Dentith M., O'Neill A. and Clark D., 2010. Ground penetrating radar as a means of studying palaeofault scarps in a deeply weathered terrain, southwestern Western Australia. *J. Appl. Geophys.*, **72**, 92–101, DOI: 10.1016/j.jappgeo.2010.07.005.

Fischer T. and Michálek J., 2008. Post 2000-swarm microearthquake activity in the principal focal zone of West Bohemia/ Vogtland: space-time distribution and waveform similarity analysis. *Stud. Geophys. Geod.*, **52**, 493–511.

Fischer T., Horálek J., Michálek J. and Boušková A., 2010. The 2008-West Bohemia earthquake swarm in the light of the WEBNET network. *J. Seismol.*, **14**, 665–682.

Flechsig C., Fabig T., Rücker C. and Schütze C., 2010. Geoelectrical investigations in the Cheb Basin/W-Bohemia: an approach to evaluate the near-surface conductivity structure. *Stud. Geophys. Geod.*, **54**, 443–463.

Havíř J., 2000. Stress analyses in the epicentral area of Nový Kostel (Western Bohemia). *Stud. Geophys. Geod.*, **44,** 522–536.

Horálek J. and Fischer T., 2010. Intraplate earthquake swarms in West Bohemia/Vogtland (Central Europe). *Jökull*, **60**, 67–88.

Kämpf H., Peterek A., Rohrmüller J., Kümpel H.J. and Geissler W., 2005. The KTB Deep Crustal Laboratory and the western Eger Graben, In: Koch R. and Röhling H.-G. (Eds.), *GeoErlangen 2005: Exkursionsführer*, *GeoErlangen 2005: System Earth - Biosphere Coupling/Regional Geology of Central Europe (Erlangen 2005)*. Schriftenreihe der Deutschen Gesellschafte für Geowissenschafte **40**, 37–107.

McClymont A.F., Villamor P. and Green A.G., 2009. Fault displacement accumulation and slip rate variability within the Taupo Rift (New Zealand) based on trench and 3-D ground-penetrating radar data. *Tectonics*, **28**, TC4005, DOI: 10.1029/2008TC002334.

Mlčoch B. and Skácelová Z., 2009. Digital elevation model of the crystalline basement of the Cheb and Sokolov Basin areas (Western Bohemia, Central Europe). *Z. Geol. Wiss.*, **37**, 145–152.

Mrlina J., Kämpf H., Kroner C., Mingram J., Stebich M., Brauer A., Geissler W.H., Kallmeyer J., Matthes H. and Seidl M., 2009. Discovery of the first Quaternary maar in the Bohemian Massif, Central Europe, based on combined geophysical and geological surveys. *J. Volcanol. Geotherm. Res.*, **182**, 97–112. DOI: 10.1016/j.jvolgeores.2009.01.027.

Pauseli C., Federico C., Frigeri A., Orosei R., Barchi M.R. and Basile G., 2010. Ground penetrating radar investigations to study active faults in the Norcia Basin (central Italy). *J. Appl. Geophys.*, **72**, 39–45.

Peterek A., Reuther C.D. and Schunk R., 2011. Neotectonic evolution of the Cheb Basin (Northwestern Bohemia, Czech Republic) and its implications for the late Pliocene to Recent crustal deformation in the western part of the Eger Rift. *Z. Geol. Wiss.*, **39**, 335–365.

Pitra P., Burg J.P. and Guiraud M, 1999. Late Variscan strike-slip tectonics between the Tepla-Barrandian and Moldanubian terranes (Czech Bohemian Massif): petrostructural evidence. *J. Geol. Soc. London*, **156**, 1003–1020.

Seht M.I., Plenefisch T. and Schmedes E, 2006. Faulting style and stress field investigations for swarm earthquakes in NE Baveria/Germany - the transition between Vogtland/NW-Bohemia and the KTB-site. *J. Seismol.*, **10**, 197–211.

Špičáková L., Uličný D. and Koudelková G., 2000. Tectonosedimentary evolution of the Cheb Basin (NW Bohemia, Czech Republic) between the Late Oligocene and Pliocene: A preliminary note. *Stud. Geophys. Geod.*, **44,** 556–580.

Štěpančíková P., Hók J., Nývlt D., Dohnal J., Sýkorová I. and Stemberk J., 2010. Active tectonics research using trenching technique on the south-eastern section of the Sudetic Marginal Fault (NE Bohemian Massif, central Europe). *Tectonophysics*, **485**, 269–282.

Štěpančíková P., Dohnal J., Pánek T., Lój M., Smolková V. and Šilhán K., 2011, The application of electrical resistivity tomography and gravimetric survey as useful tools in an active tectonics study of the Sudetic Marginal Fault (Bohemian Massif, central Europe). *J. Appl. Geophys.*, **74**, 69–80.

Valenta J., Stejskal V. and Štěpančíková P., 2008. Tectonic pattern of the Hronov-Poříčí trough as seen from pole-dipole geoelectrical measurements. *Acta Geodyn. Geomater.*, **5**, 185–195.

Vavryčuk V., 2011. Tensile earthquakes: Theory, modeling, and inversion. *J. Geophys. Res.*, **116**, B12320, DOI: 10.1029/2011JB008770.

Weinlich F., Tesař J., Weise S.M., Bräuer K. and Kämpf H., 1998. Gas flux distribution in mineral springs and tectonic structure in the western Eger Rift. *J. Czech Geol. Soc.*, **43**, 91–110.